

## Supplementary Materials

### Photothermal catalytic H<sub>2</sub> production over hierarchical porous CaTiO<sub>3</sub> with plasmonic gold nanoparticles

Xinti Yu<sup>1</sup>, Zechuan Yu<sup>2</sup>, Heng Zhao<sup>1,\*</sup>, Ian D. Gates<sup>1,\*</sup>, Jinguang Hu<sup>1,\*</sup>

<sup>1</sup>Department of Chemical and Petroleum Engineering, University of Calgary, Calgary T2N 1N4, Canada.

<sup>2</sup>Department of Wood Science, University of British Columbia, Vancouver V6T 1Z4, Canada.

\*To whom correspondence should be addressed. Email: heng.zhao1@ucalgary.ca; idgates@ucalgary.ca; jinguang.hu@ucalgary.ca

## EXPERIMENTAL MATERIALS AND METHODS

### Materials

Styrene, ethanol, tetraisopropyl titanate (TIPT), sodium hydroxide, calcium nitrate tetrahydrate, and sodium borohydride were purchased from Aldrich. Gold chloride solution was purchased from Alfa Aesar.

### Colloidal sphere preparation

Surfactant-free emulsion polymerization method was applied to prepared polystyrene (PS) spheres. Styrene was washed three times using 2 M NaOH to remove the inhibitors. Prewashed styrene (40 mL) and water (400 mL) were heated to 85°C in an oil bath under a N<sub>2</sub> atmosphere, stirring at a certain speed for 0.5 h. The initiator K<sub>2</sub>S<sub>2</sub>O<sub>8</sub> (0.4 g) was added to activate the polymerization. The reaction was stopped after 12 h by cooling the container and making the air through the system. PS template was obtained directly by low-speed centrifugation of PS spheres.

### **Preparation of 3DOM CaTiO<sub>3</sub>**

The precursor was composed of ethanol (20 mL), Ca(NO<sub>3</sub>)<sub>2</sub> 5.9 g, 0.025 mol), nitric acid (1.5 mL), titanium (IV) isopropoxide (7.4 mL, the molar ratio of Ca:Ti is 1:1) and water (2 mL). The mixture was added to a beaker and stirred at room temperature for 5 mins. The dried PS template (5 g) was placed on filter paper in a Buchner funnel, and the precursor was added to the PS templates during suction applied to the Buchner funnel. After air drying the mixture of precursor and template for 48 h, the sample was stabilized at 300 °C for 2 h, 400 °C for 2 h and 550 °C for 2 h using a heating rate 2 °C/min in atmosphere. The obtained white powder was washed with dilute nitric acid to remove the trace amounts of CaCO<sub>3</sub>.

### **Decoration of Au nanoparticles on the 3DOM CaTiO<sub>3</sub>**

0.2 g of CaTiO<sub>3</sub> was immersed into 40 mL of HAuCl<sub>4</sub> aqueous solution (0.2 mg/mL) with vigorous stirring for 0.5 h. 6 mg of trisodium citrate was added as stabilizer of Au nanoparticles. 2.4 mL of sodium borohydride aqueous solution (0.1 mmol/mL) was added to reduce Au<sup>3+</sup>. The mixture was stirred for another 2 h and the dark purple 3DOM Au-CaTiO<sub>3</sub> was obtained after filtration.

### **Characterization**

The sample morphology and structure of the 3DOM were observed with a field-emission scanning electron microscope (SEM, Hitachi S-4800) with an energy-dispersive X-ray (EDX) analysis system and a transmission electron microscope (TEM, JEOL JEM 2100F). The crystalline phase of the samples was examined by powder X-ray diffraction (XRD, D8 ADVANCE) equipped with a Cu anode X-ray tube (Cu K $\alpha$ X-rays,  $\lambda = 1.54056\text{\AA}$ ). X-ray photoelectron spectroscopy (XPS) was worked out with a customized X-ray photoelectron spectrometer (VG Multilab 2000-X equipped with a monochromatic Al K $\alpha$  source) and all the results have been calibrated by the C 1s at 284.8 eV. The UV-vis absorption spectra were collected by SHIMADZU UV-vis spectrophotometer in the spectral range 200-800nm. Photoluminescence (PL) spectra were recorded using a fluorescence

spectrophotometer (Perkin-Elmer LS-55) and the excitation wavelength was set at 400 nm. The actual content of gold was measured by an inductively coupled plasma emission spectrometer (ICP-AES, PerkinElmer Optima 4300DV). The oxygen vacancy was measured by electron paramagnetic resonance (EPR) on JES-X320 (JEOL).

### **Photothermal catalytic H<sub>2</sub> evolution**

The photothermal catalytic reactions were carried out in a closed glass vial with a total volume of 20 mL. 10 mg of the catalyst was mixed with 10 mL of 5 vol% glycerol aqueous solution. The suspension was sonicated for 10 min to disperse the catalyst well, during which the reactor was connected to a pump with a needle to vacuum the system for 0.5 h. The reactor was then placed on a heating and stirring plate with the irradiation by a 300 W Xenon lamp (Excelitas Tech.). The gas-phase products were periodically collected and analyzed by a gas chromatography (GC, PerkinElmer Clarus 590) with a Molecular Sieve 5A packed column and a Carboxen 1000 packed column. The detectors are a thermal conductivity detector (TCD) and a flame ionization detector (FID). The liquid-phase products were periodically collected and analyzed by a high-performance liquid chromatography (HPLC) which was equipped with an Aminex HPX-87H (300 × 7.8 mm, Bio-Rad) column and a refractive index detector (RID). The same volume ratio of other liquid substrates (methanol, ethanol, ethylene glycerol) and 10 g/L of solid substrates (glucose, cellobiose and avicel) were applied accordingly to check the hydrogen production.

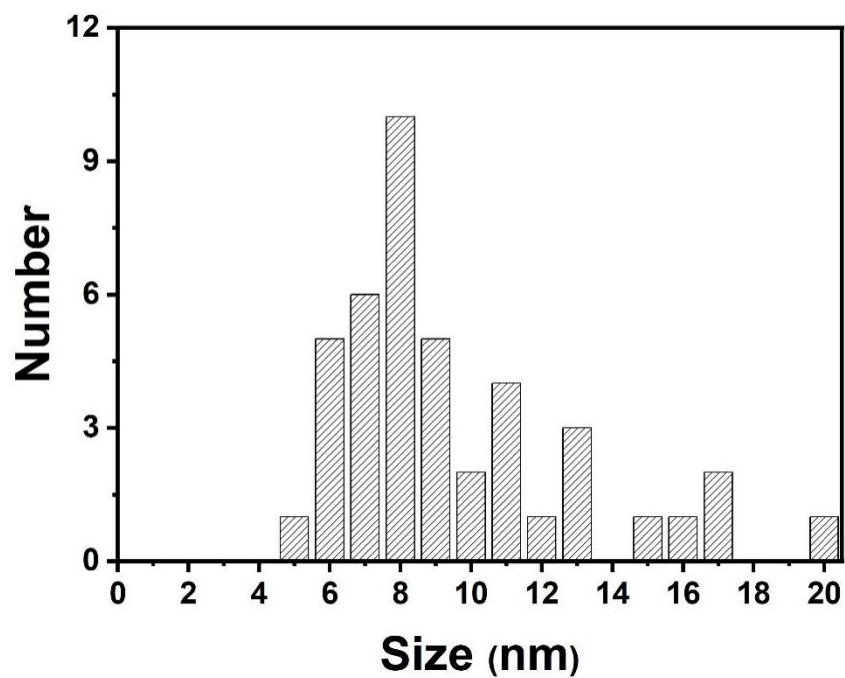
### **Density functional theory**

A density functional theory (DFT) calculation is performed with CP2K<sup>[1]</sup>. The input script and post-processing are completed with Multiwfn<sup>[2]</sup>. The calculation yields an electronic density difference at the interface between perovskite and gold. The perovskite is modeled by a (1 1 0) surface of a cubic unit cell, spanning a periodic  $xy$  plane<sup>[3]</sup>. The gold is modeled by an FCC unit cell with its (1 1 1) surface exposed to the perovskite substrate. Cell optimization is performed in  $x$  and  $y$  directions with a

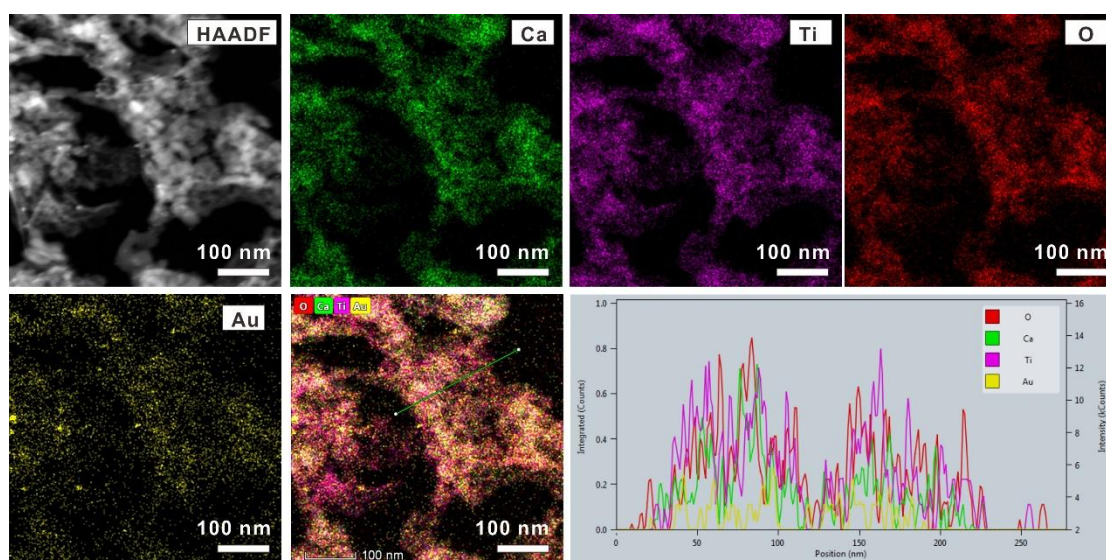
perovskite supercell spanning (0 0 2) and (2 -2 0) of the original unit cell, with a thickness of 2.5 times of the original unit cell in the (1 1 0) direction. Six gold atoms are placed above the optimized perovskite structure, and then a geometry optimization is performed. The electronic density difference is calculated by subtracting the wavefunction of the compound from the wavefunction of two individual components (gold and perovskite) and further evaluating the obtained wavefunction in real space. Consequently, regions with positive or negative values indicate enriched or reduced electronic distribution brought by the addition of gold. All the DFT calculation is performed at the level of DZVP-MOLOPT-SR-GTH basis set, with PBE the exchange-correlation function, GTH-PBE the pseudo potential, an energy cutoff of 350 eV and a 15-Å vacuum space in the  $z$  direction. Visualization of the electronic density difference is done by OVITO<sup>[4]</sup>.

Based on the perovskite-gold model, we add two oxygen atoms near gold to simulate the existence of gold ions as observed from experiments. Hirshfeld atomic charges of gold are calculated before and after the addition of oxygen atoms. The Hirshfeld atomic charges are about -0.06 e for the two upper-layer gold atoms, and about +0.02 e for the four bottom-layer gold atoms. With the two additional oxygen atoms, the charges rise to about +0.23 e for the upper-layer and about +0.06 e for the bottom-layer gold atoms. This increase in atomic charges indicates a reduced electron population around gold due to the additional oxygen atoms, which can help simulate the presence of gold ions at the perovskite interface. We hypothesize that the gold ions raise ambient electrostatic potential and make the trapping of proton less favorable, compared to the gold atom. The difference in electrostatic potential distributed near the binding site of proton is calculated and analyzed<sup>[5]</sup>.

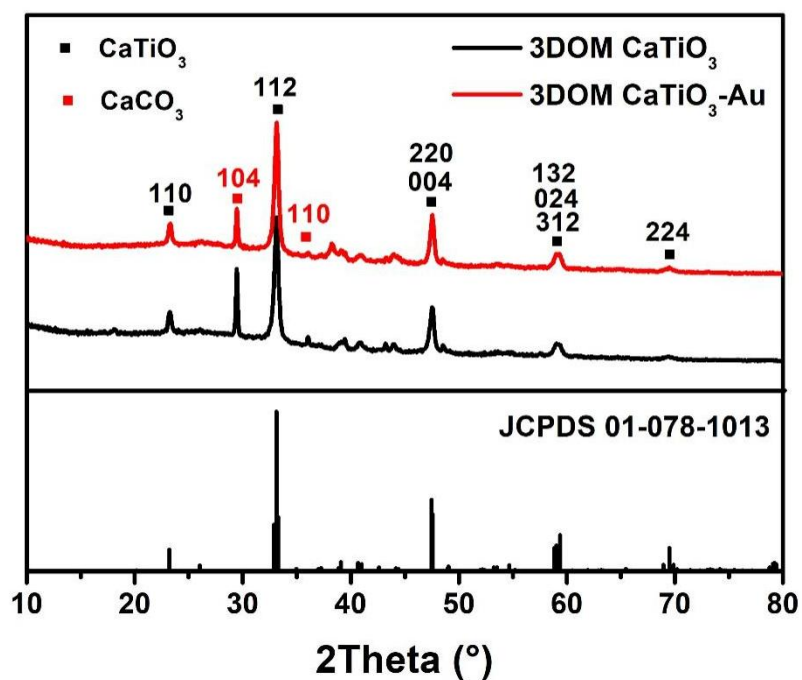
## SUPPORTING FIGURES



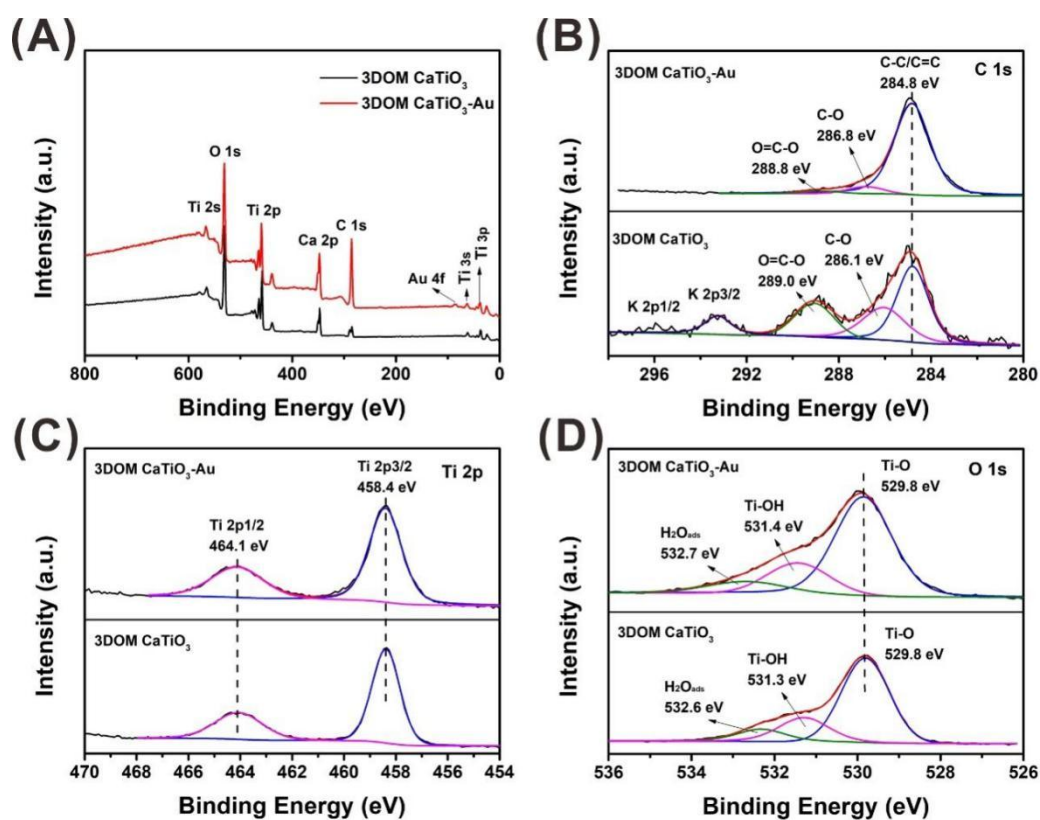
**Supplementary Figure 1.** Statistical analysis of the size of gold nanoparticles in 3DOM CaTiO<sub>3</sub>-Au.



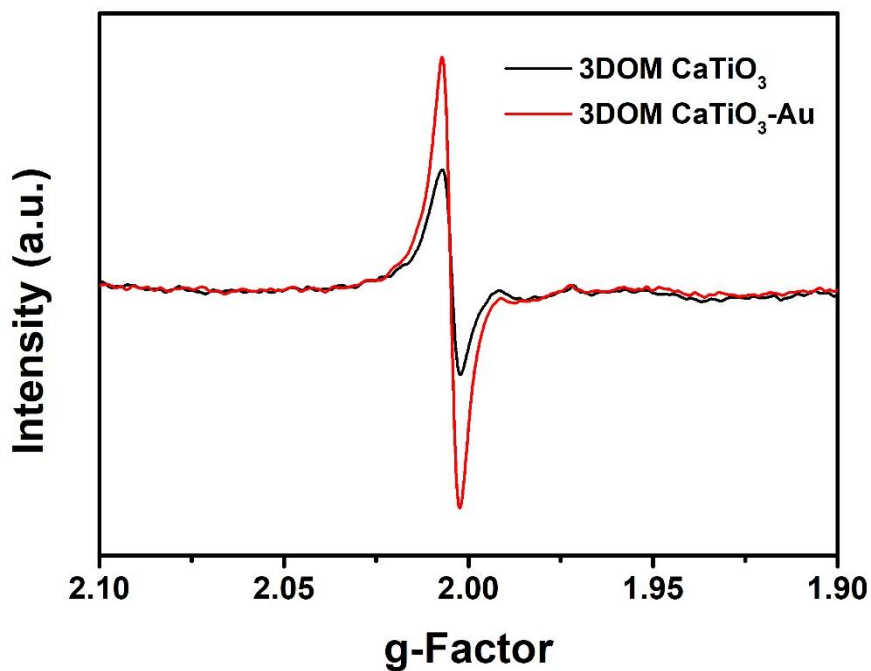
**Supplementary Figure 2.** HAADF and corresponding element mappings of 3DOM CaTiO<sub>3</sub>-Au.



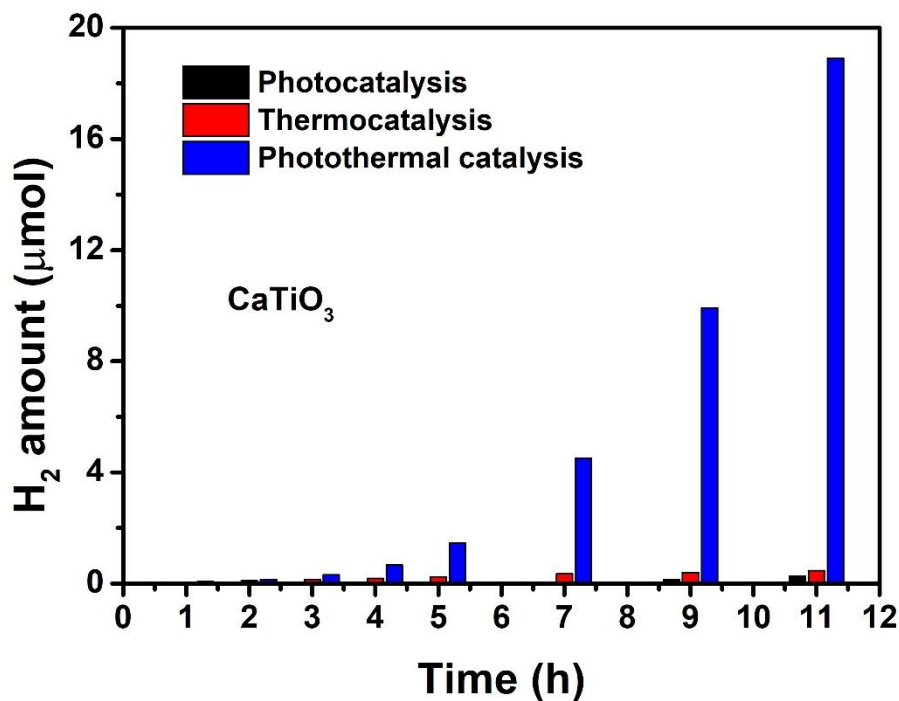
**Supplementary Figure 3.** XRD patterns of 3DOM  $\text{CaTiO}_3$  and 3DOM  $\text{CaTiO}_3\text{-Au}$  without washing by diluted nitric acid.



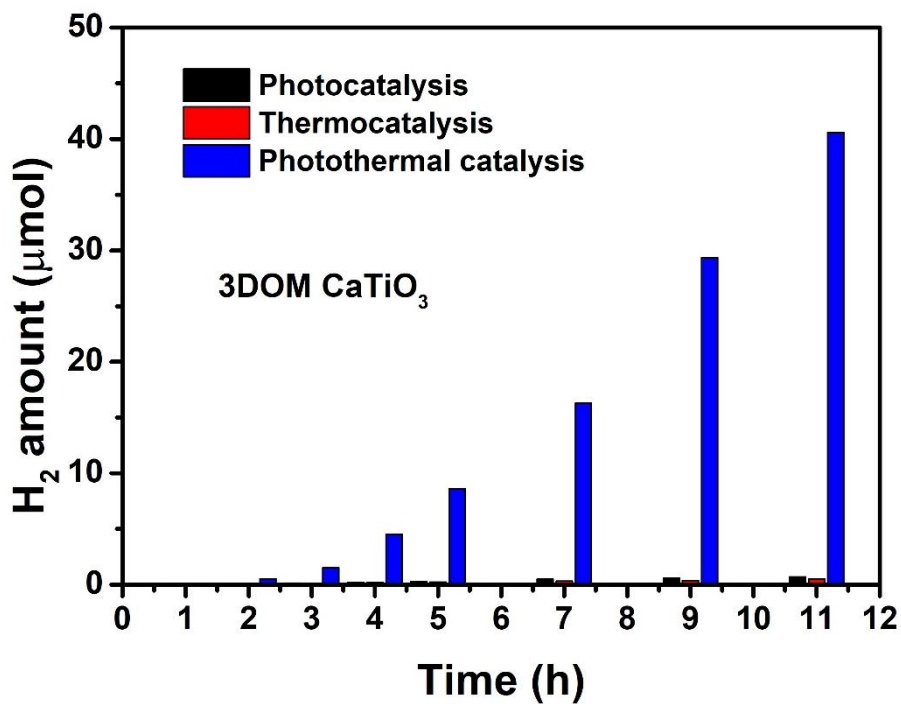
**Supplementary Figure 4.** (A) General survey scan, high-resolution spectra of (B) C 1s, (C) Ti 2p and (D) O 1s.



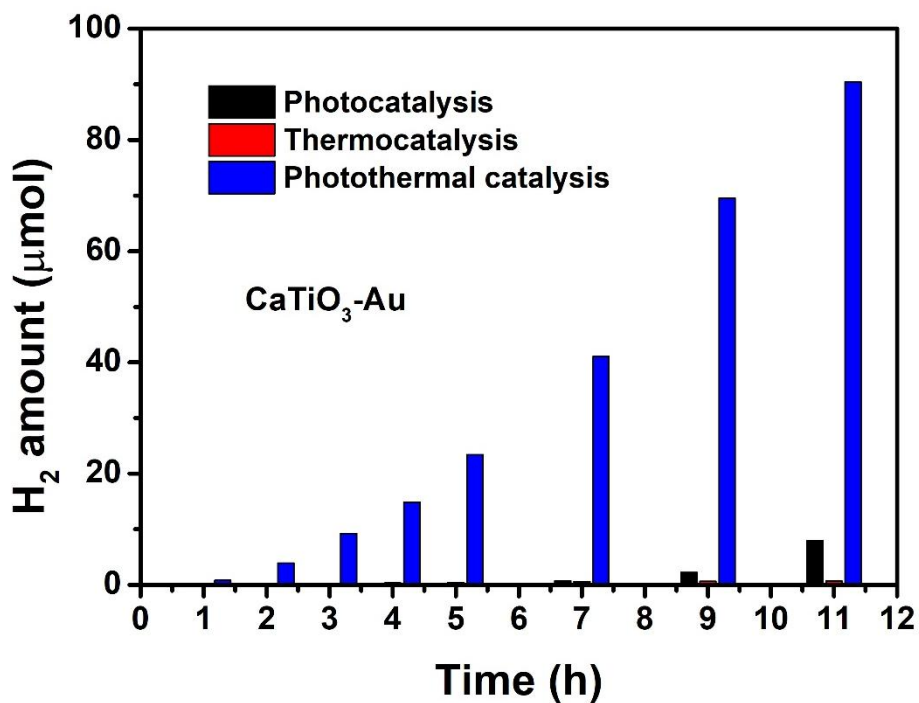
Supplementary Figure 5. EPR spectra of oxygen vacancy for 3DOM CaTiO<sub>3</sub> and 3DOM CaTiO<sub>3</sub>-Au.



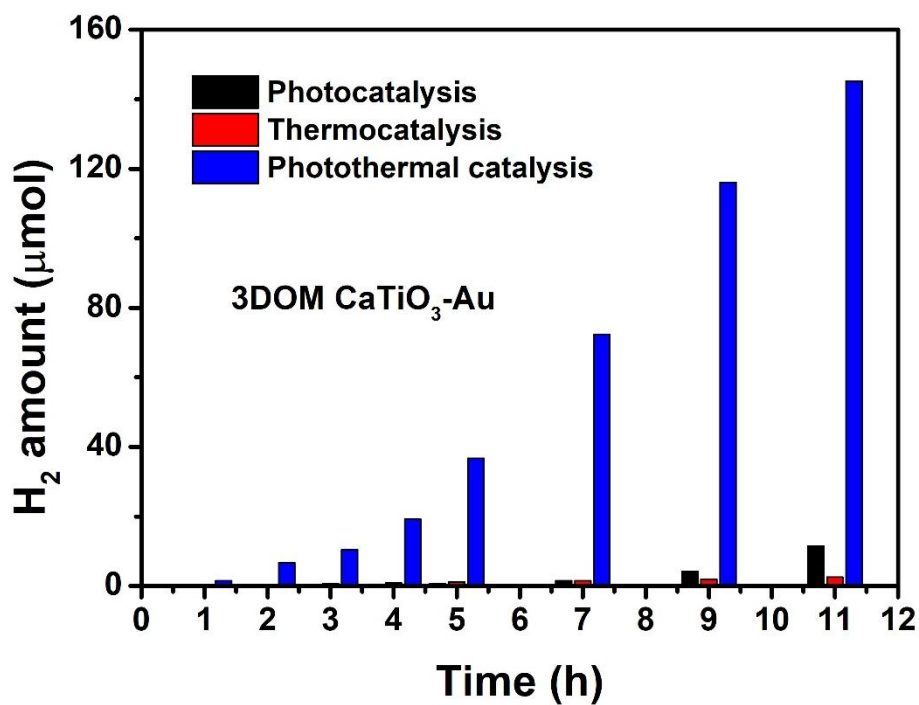
Supplementary Figure 6. The comparison of H<sub>2</sub> production over CaTiO<sub>3</sub> by different reaction approaches.



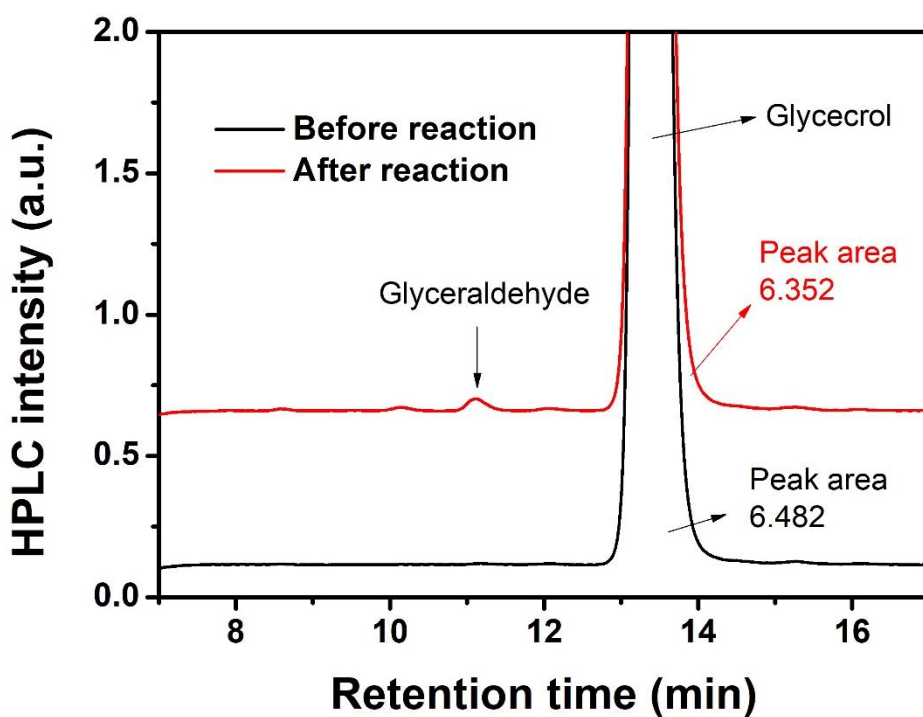
Supplementary Figure 7. The comparison of H<sub>2</sub> production over 3DOM CaTiO<sub>3</sub> by different reaction approaches.



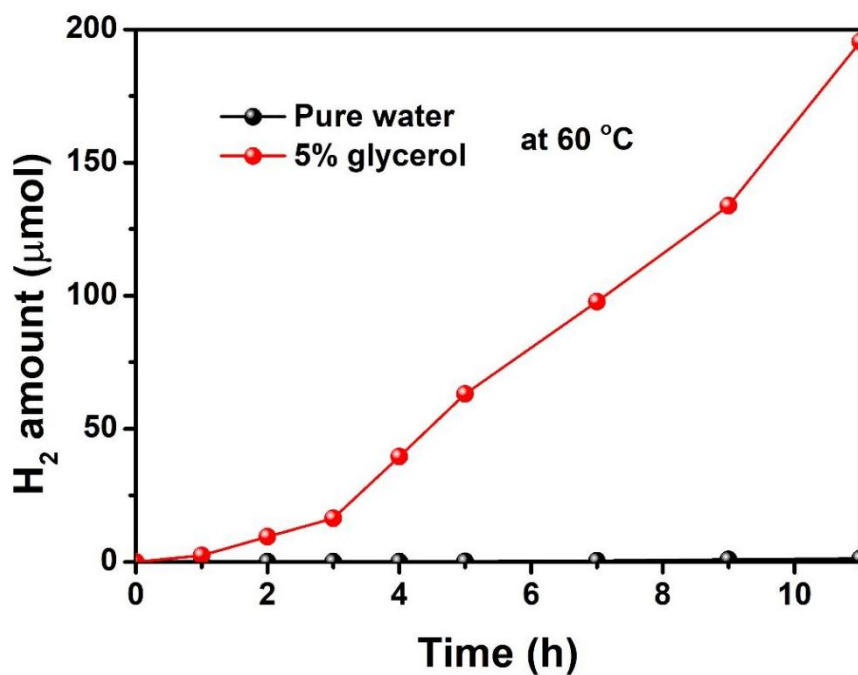
Supplementary Figure 8. The comparison of H<sub>2</sub> production over CaTiO<sub>3</sub>-Au by different reaction approaches.



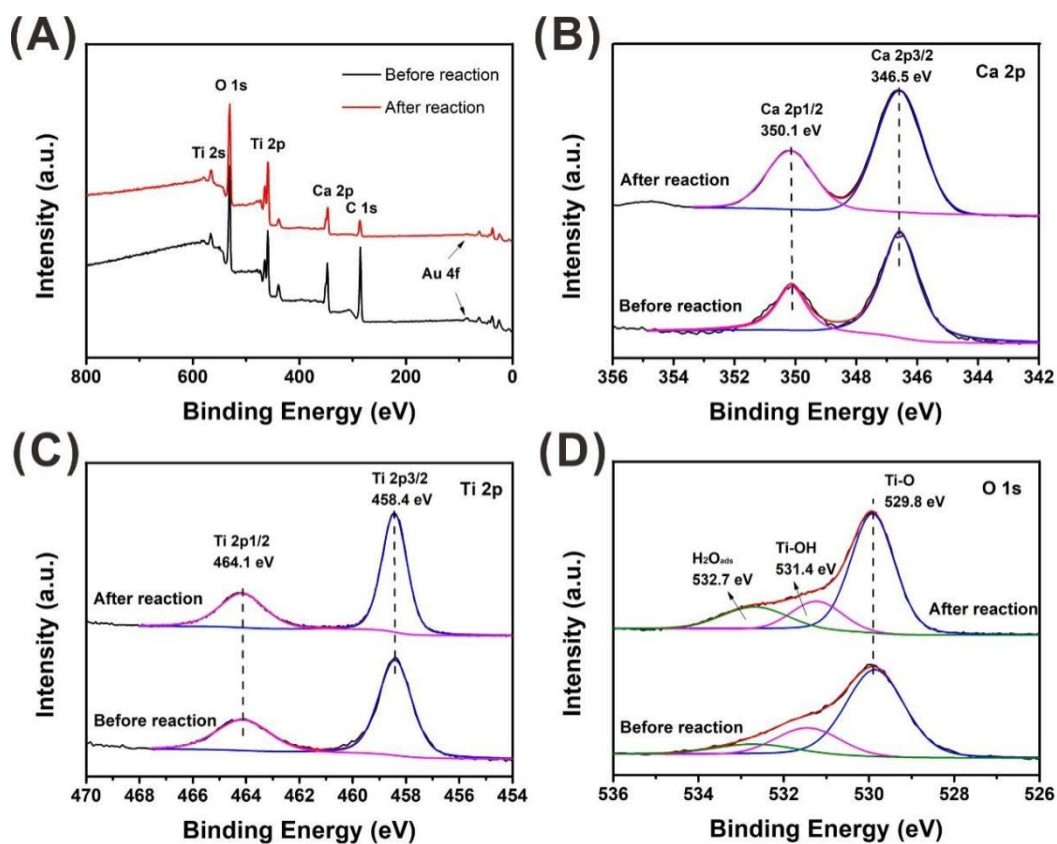
Supplementary Figure 9. The comparison of H<sub>2</sub> production over 3DOM CaTiO<sub>3</sub>-Au by different reaction approaches.



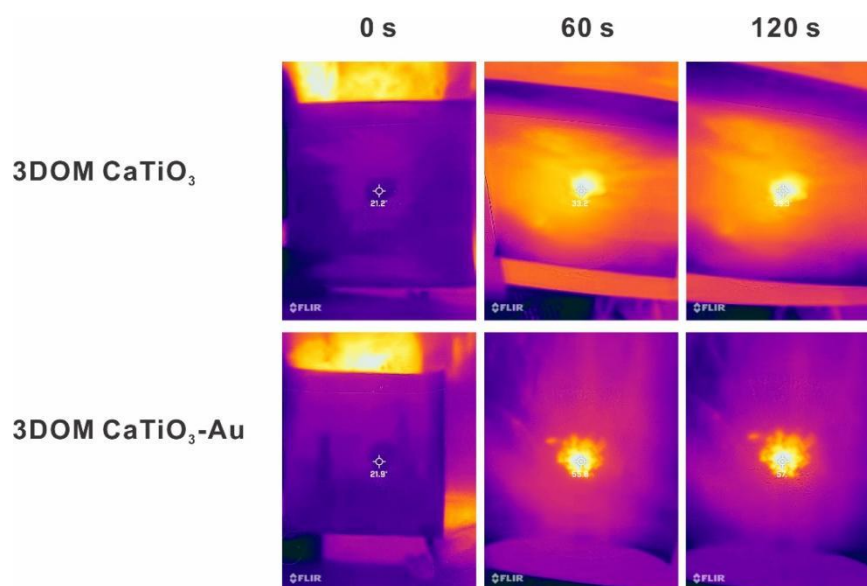
Supplementary Figure 10. HPLC signal of liquid product distribution before and after reaction.



**Supplementary Figure 11.** H<sub>2</sub> production over 3DOM CaTiO<sub>3</sub>-Au in pure water and 5 vol% glycerol by photothermal catalysis at 60 °C.



**Supplementary Figure 12.** (a) General survey scan, high-resolution spectra of (b) Ca sp, (c) Ti 2p, (d) O 1s of 3DOM CaTiO<sub>3</sub>-Au before and after catalytic reaction.



**Supplementary Figure 13.** The recorded IR thermal images with different light irradiation times for 3DOM CaTiO<sub>3</sub> and 3DOM CaTiO<sub>3</sub>-Au.

## SUPPORTING TABLES

**Supplementary Table 1. Experiment data of H<sub>2</sub> amount for each catalyst**

Time (h)	H <sub>2</sub> production (μmol)											
	Thermo-				Photo-				Thermo-photo-			
	(1)	(2)	(3)	(4)	(1)	(2)	(3)	(4)	(1)	(2)	(3)	(4)
1	0.04	0.09	0.13	0.13	0.01	0.03	0.01	0.14	0.07	0.10	0.80	1.49
	3	8	3	3	6	3	8	2	6	3	4	4
2	0.10	0.11	0.16	0.34	0.02	0.08	0.03	0.18	0.15	0.52	3.91	6.65
	3	8	6	8	2	0	8	4	6	2	3	8
3	0.15	0.12	0.25	0.61	0.02	0.14	0.08	0.36	0.31	1.52	9.28	10.4
	3	0	3	7	5	5	0	0	5	1	2	3
4	0.19	0.20	0.36	0.90	0.02	0.21	0.11	0.47	0.67	4.53	14.8	19.1
	6	7	1	7	8	4	9	9	5	5	5	7
5	0.25	0.24	0.42	1.15	0.02	0.30	0.21	0.68	1.45	8.60	23.3	36.6
	2	4	6	4	9	0	6	6	4	5	9	7
7	0.35	0.31	0.62	1.53	0.03	0.49	0.71	1.49	4.52	16.3	41.1	72.4
	1	5	6	6	3	0	0	2	2	1	0	3
9	0.39	0.40	0.63	1.90	0.16	0.57	2.22	4.25	9.92	29.3	69.5	116.
	6	2	0	4	0	9	6	1	8	7	1	1
11	0.46	0.52	0.72	2.54	0.26	0.70	7.89	11.5	18.9	40.6	90.4	145.
	8	2	7	7	1	4	2	7	1	0	1	2

(1): CaTiO<sub>3</sub>; (2): 3DOM CaTiO<sub>3</sub>; (3): CaTiO<sub>3</sub>-Au; (4): 3DOM CaTiO<sub>3</sub>-Au. Raw data for Figure 3A-C in the manuscript.

**Supplementary Table 2. Hydrogen production compared with the literature**

Entry	Catalyst	Reaction mode	Reaction condition	H <sub>2</sub> evolution (mmol/h/g)	Ref.
1	3DOM CaTiO <sub>3</sub> -Au	Photothermal catalysis	1 vol% glycerol	1.88	This work
2	2D Au/TiO <sub>2</sub> nanoflakes	Photothermal catalysis	10 vol% glycerol	2.38	[6]
3	Cu@Ni/g-C <sub>3</sub> N <sub>4</sub>	Photothermal	20 vol%	0.055	[7]

		catalysis	triethanolamine		
4	FeS <sub>2</sub> @ZnIn <sub>2</sub> S <sub>4</sub>	photothermal-assisted photocatalysis	10 vol% triethanolamine	5.05	[8]
5	3DOM CQDs-CaTiO <sub>3</sub>	Photocatalysis	50 vol% methanol	0.13	[9]
6	Ag(0)/CaTiO <sub>3</sub>	Photocatalysis	10 vol% glycerol	0.17	[10]
7	Cu-CaTiO <sub>3</sub>	Photocatalysis	20 vol% methanol	0.25	[11]
8	CaTiO <sub>3</sub> nanosheets	Photocatalysis	50 vol% methanol	2.30	[12]
9	MoS <sub>2</sub> /CaTiO <sub>3</sub>	Photocatalysis	0.3 M vitamin C	0.62	[13]

## REFERENCE

1. Kuhne TD, Iannuzzi M, Del Ben M, et al. Cp2k: An electronic structure and molecular dynamics software package - quickstep: efficient and accurate electronic structure calculations. *J Chem Phys* 2020; 152: 194103. DOI: 10.1063/5.0007045
2. Lu T, Chen FW. Multiwfn: A multifunctional wavefunction analyzer. *J Comput Chem* 2012; 33: 580-92. DOI: 10.1002/jcc.22885
3. Balachandran J, Lin LS, Anchell JS, Bridges CA, Ganesh P. Defect genome of cubic perovskites for fuel cell applications. *J Phys Chem C* 2017; 121: 26637-47. DOI: 10.1021/acs.jpcc.7b08716
4. Stukowski A. Visualization and analysis of atomistic simulation data with ovito- the open visualization tool. *Model Simul Mater Sc* 2010; 18: 015012. DOI: 10.1088/0965-0393/18/1/015012
5. Zhang J, Lu T. Efficient evaluation of electrostatic potential with computerized optimized code. *Phys Chem Chem Phys* 2021; 23: 20323-28. DOI: 10.1039/d1cp02805g
6. Zhong WL, Wang C, Zhao HL, et al. Synergistic effect of photo-thermal catalytic glycerol reforming hydrogen production over 2D Au/TiO<sub>2</sub> nanoflakes. *Chem Eng J*

2022; 446: 137063. DOI: 10.1016/j.cej.2022.137063

7. Guo XY, Xue F, Xu SK, et al. Coupling photothermal effect into efficient photocatalytic H<sub>2</sub> production by using a plate-like Cu@Ni core-shell cocatalyst.

*ChemCatChem* 2020; 12: 2745-51. DOI: 10.1002/cctc.202000258

8. Chen KY, Shi YX, Shu P, et al. Construction of core-shell FeS<sub>2</sub>@ZnIn<sub>2</sub>S<sub>4</sub> hollow hierarchical structure S-scheme heterojunction for boosted photothermal-assisted photocatalytic H<sub>2</sub> production. *Chem Eng J* 2023; 454: 140053. DOI: 10.1016/J.Cej.2022.140053

9. Zhao H, Liu J, Li CF, et al. Meso-microporous nanosheet-constructed 3DOM perovskites for remarkable photocatalytic hydrogen production. *Adv Funct Mater* 2022; 32: 2112831. DOI: 10.1002/Adfm.202112831

10. Alzahrani A, Barbash D, Samokhvalov A. "One-pot" synthesis and photocatalytic hydrogen generation with nanocrystalline Ag<sub>0</sub>/CaTiO<sub>3</sub> and in situ mechanistic studies. *J Phys Chem C* 2016; 120: 19970-79. DOI: 10.1021/acs.jpcc.6b05407

11. Lu MJ, Liu SY, Xiong JY, Li W. Facilely coupling CaTiO<sub>3</sub> nanorods with Cu nanoparticles for enhanced photocatalytic hydrogen evolution through efficient charge separation. *Inorg Chem Commun* 2022; 139: 109377. DOI: 10.1016/J.Inoche.2022.109377

12. Cai JM, Cao A, Huang JJ, et al. Understanding oxygen vacancies in disorder-engineered surface and subsurface of CaTiO<sub>3</sub> nanosheets on photocatalytic hydrogen evolution. *Appl Catal B-Environ* 2020; 267: 118378. DOI: 10.1016/J.Apcatb.2019.118378

13. Jiang EH, Song N, Che GB, et al. Construction of a Z-scheme MoS<sub>2</sub>/CaTiO<sub>3</sub> heterostructure by the morphology-controlled strategy towards enhancing photocatalytic activity. *Chem Eng J* 2020; 399: 125721. DOI: 10.1016/J.Cej.2020.125721